Journal of Materials Chemistry A

ROYAL SOCIETY OF CHEMISTRY

PAPER

View Article Online
View Journal | View Issue

Check for updates

Cite this: J. Mater. Chem. A, 2023, 11, 16838

Controlling the metal–support interaction with steam-modified ceria to boost Pd activity towards low-temperature CO oxidation†

Yuanyuan An,[a] Sheng-Yu Chen,[a] Beibei Wang,[b] Li Zhou,[a] Guoxiu Hao,[a] Yanli Wang,[a] Junchen Chen,[a] Chia-Kuang Tsung,[‡c] Zhi Liu*[abd] and Lien-Yang Chou*[a]

Received 3rd May 2023
Accepted 12th July 2023

DOI: 10.1039/d3ta02626d

rsc.li/materials-a

The performance of cerium-based composite catalysts can be improved by regulating the metal–support interaction (MSI) through the modification process. Unlike common steam post-modification, this study reveals that the steam treatment of the ceria support before loading palladium can significantly reduce the activation energy (11.6 kJ mol^{-1}) of the composite catalyst (Pd_A-ST) for CO oxidation, and achieve high catalytic activity at low temperature (9.72 mol_{CO} h^{-1} g_{Pd}^{-1}, 27 °C). Thermally stable hydroxyl groups (OH) are generated on the ceria surface due to the dissociation of high-temperature steam at oxygen vacancies. The OH-modified ceria affects the loaded palladium in three aspects, including MSI enhancement, metal dispersion promotion and the binding energy shift of active Pd^{2+} species. Strong MSI often causes strong CO adsorption, resulting in catalyst poisoning at low temperatures. However, low binding strength between palladium and CO molecules was found in this study, leading to high catalytic activity at low temperature. This study provides an example of the regulation of MSI to obtain high-performance catalysts and demonstrates the potential of developing effective catalysts for low-temperature catalytic reactions.

1. Introduction

Cerium-based noble metal catalysts are widely used in heterogeneous catalysis.[1–4] As a common reducible oxide support, cerium oxide not only has a rich defect concentration and high-temperature stability but also has a strong interaction with transition metals.[1,4] This interaction enables ceria to stabilize small-sized metals, regulate the metal's electronic structure, and assist in redox reactions.[5–7] Many studies have focused on improving performance and expanding the applications of cerium-based catalysts through various strategies, including morphology control, doping, and catalyst post-modification.[8–12]

Post-modification engineering, especially water post-treatment, is considered to be an effective way to improve the activity and stability of cerium-based catalysts.[11–14] Taking the common cerium-based platinum-group catalysts as an example, Wang *et al.*[14] observed that OH groups and more active lattice oxygen were generated near the Pt sites after a high-temperature steam treatment on the Pt/CeO_2 catalyst. The active oxygen species were proved to reduce the reaction energy barrier and improve the activity for CO oxidation. Lee *et al.*[11] found that hydroxyl groups formed after a similar steam treatment on Pd/CeO_2 can inhibit the formation of carbonates, preventing them from poisoning the catalyst, and thereby improving the stability of the composite catalyst. Li *et al.*[12] pointed out that the steam treatment of Pt/CeO_2 can remove part of the lattice oxygen and form oxygen vacancies, which was beneficial to activate the C–H bond in the methane oxidation process. During the process of steam treatment modification, water molecules usually interact with cerium oxide to form OH groups accompanied by the re-dispersion of the loaded previous metal due to the high-temperature process and strong metal–support interaction (MSI). These adjustments are definitely beneficial for the ceria support and loaded precious metals. However, the influence of the support modification on the precious metal reloading process remains unclear. Further research on steam treatment modification is therefore needed and may pave a way to improve the performance of cerium-based noble metal catalysts.

In this study, we performed a steam modification of the ceria support before metal loading and investigated the optimal modification conditions. The prepared Pd–CeO_2 composite catalyst exhibited an ultrahigh activity for CO oxidation (9.72

[a]School of Physical Science and Technology, ShanghaiTech University, Shanghai 201210, China. E-mail: zhuoly@shanghaitech.edu.cn; liuzhi@shanghaitech.edu.cn
[b]Center for Transformative Science, ShanghaiTech University, Shanghai 201210, China
[c]Department of Chemistry, Boston College, Chestnut Hill, Massachusetts, 02467, USA
[d]Shanghai high repetition rate XFEL and extreme light facility (SHINE), ShanghaiTech University, Shanghai 201210, China

† Electronic supplementary information (ESI) available. See DOI: https://doi.org/10.1039/d3ta02626d

‡ Deceased, January 5, 2021.

$mol_{CO}\ h^{-1}\ g_{Pd}{}^{-1}$ at 27 °C), surpassing most reported Pd- and Pt-catalysts, even the steam-treated samples after Pd or Pt loading in the literature.[11,14–20] *In situ* photoelectron spectroscopy was used to analyze the relationship between steam and ceria. We found that OH groups were formed on the defects of ceria, which were more stable than the residual OH groups that were formed synthetically. The steam modification process will influence the properties of ceria to regulate MSI. This modulation on the ceria support was verified to further affect the dispersion and valence states of the loaded metal, as well as the interaction with reactant molecules.

2. Results and discussion

2.1 Exploring steam treatment conditions and test performance

Water molecules are considered to be dissociated and form OH groups on the reduced surface of ceria at high temperatures.[14,21,22] Ceria nanorods were synthesized following the reported hydrothermal method[7] and referred to as A-CeO_2 (Step 1 in Fig. S1†). We then modified A-CeO_2 through steam (2 vol%) treatment (ST) before loading metals (Step 2). The ST process of A-CeO_2 was carried out at 450 °C, as oxygen vacancies of ceria could move around when the temperature exceeds 400 °C.[23] Pd was subsequently loaded onto the ceria support by the wet chemical method and completely dispersed by calcination under an oxygen atmosphere[24–26] (Step 3). The obtained composite sample with the ST process was denoted as Pd_A-ST-450. Two other samples, Pd_A-450 (450 °C calcination, no steam) and Pd_A (no calcination, no ST), were also prepared as controls. CO oxidation was conducted as a probe reaction in a mixed feed gas comprising 2% CO with 20% O_2 to evaluate catalyst performance. The results showed that the T_{50} (the temperature at 50% CO conversion) of Pd_A-ST-450 (64 °C) was approximately 40 °C lower than that of Pd_A-450 (102 °C) and Pd_A (106 °C), demonstrating that the ST process of ceria can effectively enhance the activity of the composite catalyst (Fig. S2a†). Subsequently, we studied the temperature effect of ST (Fig. S2b†). With the increase of ST temperature, the activity of the Pd–CeO_2 composite catalyst can be further improved, and a significant enhancement can be observed above 600 °C. It is noteworthy that the Pd_A-ST-750 sample exhibited low-temperature catalytic activity (2.79 $mol_{CO}\ h^{-1}\ g_{Pd}{}^{-1}$ at 22 °C) more than four times that of the Pd_A (0.589 $mol_{CO}\ h^{-1}\ g_{Pd}{}^{-1}$ at 22 °C). These results suggest that high-temperature and steam treatment on the ceria support are both required to enhance the performance of the composite catalyst. Thus, we chose 750 °C for the ST process condition, unless otherwise specified in the following sections.

The defects of the ceria may play a crucial role in steam modification as OH formation sites. To confirm that the presence of oxygen defects of ceria is crucial for the ST process, we performed ST on ceria with different defect concentrations at 750 °C and evaluated their performance. The defect concentration is often measured by the ratio ($I_D/I_{F_{2g}}$) in the Raman spectrum of the intensity of the defect-related peak (595 cm^{-1}, I_D) and the Ce–O F_{2g} related peak (460 cm^{-1}, $I_{F_{2g}}$).[19,27,28] As shown in Fig. S3,† the defect concentration of the polyhedral ceria (I_D/

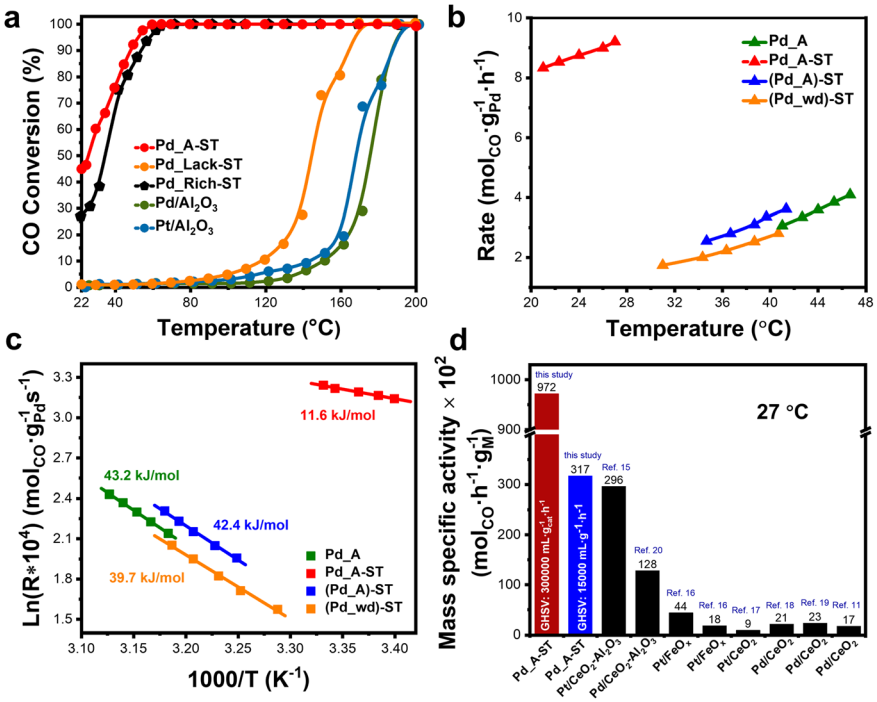

Fig. 1 (a) Comparison of catalytic performance of Pd_A-ST, Pd_Lack-ST, Pd_Rich-ST, Pd/Al_2O_3 (1% Pd, Alfa Aesar), and Pt/Al_2O_3 (1% Pt, Alfa Aesar) for CO oxidation. The gas hourly space velocity (GHSV) is 15 000 mL h^{-1} $g_{cat.}{}^{-1}$. (b) The reaction rate for CO oxidation and (c) corresponding Arrhenius plots for E_a of Pd_A-ST, Pd_A, (Pd_A)-ST, and (Pd_wd)-ST. The GHSV is 100 000 mL h^{-1} $g_{cat.}{}^{-1}$. (d) Comparison of the reported Pd-/Pt-catalysts and Pd_A-ST for CO oxidation.

$I_{F_{2g}} = 0.01$), named as Lack-CeO_2, was significantly lower than that of the rod-like A-CeO_2 ($I_D/I_{F_{2g}} = 0.07$). Following ST modification and Pd loading, the composite catalyst (Pd_Lack-ST) derived from Lack-CeO_2 exhibited significantly lower activity ($T_{\text{initial activity}}$: 80 °C) than Pd_A-ST ($T_{\text{initial activity}}$: 22 °C) (Fig. 1a), and its activity was comparable to those of the two commercial samples (Pd/Al_2O_3 and Pt/Al_2O_3) indicating no significant effect of ST on low defect ceria. To further confirm that the ST process requires defects in ceria, commercial cerium oxide nanorods with rich oxygen vacancies (Fig. S4†) were subjected to the ST process to obtain Pd_Rich-ST. Similar activities were observed for Pd_Rich-ST and Pd_A-ST (Fig. 1a). These findings demonstrate that a certain defect concentration and high-temperature ST conditions are prerequisites for ceria as a support to achieve highly active Pd catalysts.

The properties of supports can influence MSI and, consequently, impact the stability of the loaded metal.[6,29–31] For instance, electron microscopy and energy dispersive spectroscopy of fresh Pd_A-ST and Pd_Lack-ST samples, prepared by calcination in oxygen to disperse Pd, revealed no detectable Pd particles (Fig. S5a and c†). This reflects that the size of Pd on both samples is smaller than the detection limit of the instrument, indicating that the Pd is well dispersed on the two distinct supports in the initial state. However, after catalysis, Pd nanoparticles (~200 nm) caused by aggregation can be clearly observed on the Pd_Lack-ST (Fig. S5d†), but still not on Pd_A-ST (Fig. S5b†). This result can be attributed to the different MSI of Pd_A-ST and Pd_Lack-ST. The stronger MSI of Pd_A-ST can reduce the aggregation tendency of Pd atoms, thereby hindering the formation of Pd nanoparticles. In addition, the weak MSI of Pd_Lack-CeO_2 leads to the relative instability of loaded Pd, which agglomerates to ~200 nm nanoparticles during the catalysis, resulting in a significant decrease in the activity of CO oxidation in the second cycle. This is reflected as an increase in T_{50} of about 25 °C in T_{50} of Pd_Lack-CeO_2, while the catalytic curves of the Pd_A-ST in the two cycles are almost the same, representing stable performance and showing the potential of reusability (Fig. S6†). To further explore the relationship between the Pd properties and the stable catalytic performance of Pd_A-ST, X-ray photoelectron spectroscopy (XPS) was conducted to test the change of Pd species before and after the reaction (Fig. S7†). The binding energies (BE) of Pd $3d_{5/2}$ at ~337.8 eV, ~336 eV, and ~335 eV were assigned to Pd^{2+}, the semi-oxidized state ($Pd^{\delta+}$), and the metallic state (Pd^0), respectively.[29,31,32] The results showed that the Pd species were fully oxidized (Pd^{2+}) before the reaction, but 29.2% partially reduced to $Pd^{\delta+}$ and Pd^0 after the reaction. However, the catalytic activity of the Pd_A-ST did not decay in the following catalysis, reflecting that the change of the Pd valence state had little effect on the activity of Pd_A-ST. These results illustrate the profound impact of the regulation of support properties.

Although post-water treatment on ceria-based composite catalysts has shown catalytic performance enhancement,[11,14] the ST process on the ceria support before Pd loading appears to exhibit higher activity, particularly in the low-temperature region. To confirm if the sequence of the ST process has any different effects on the performance improvement of the Pd–CeO_2 composite catalyst, samples with the ST process before and after loading metals were compared. The synthetic processes of the samples are illustrated in Fig. S8,† which include loading Pd on ceria with ST (Pd_A-ST), without ST (Pd_A), and two conditions of ST after Pd loading: loading Pd with the metal dispersion process ((Pd_A)-ST) and without the dispersion process ((Pd_wd)-ST). The catalytic results indicated that the CO oxidation of Pd_A-ST was significantly higher than that of the other three samples (Fig. 1b and S9†). Pd_A-ST achieved a high conversion of 15.5%, and the reaction rate was 8.5 $mol_{CO}\ h^{-1}\ g_{Pd}{}^{-1}$, which was at least five times greater than that of the other three samples at 22 °C. The activation energy (E_a) of the catalysts was calculated using the Arrhenius plots (Fig. 1c). The E_a of Pd_A-ST (11.6 kJ mol^{-1}) was significantly lower than that of Pd_A (43.2 kJ mol^{-1}), (Pd_A)-ST (42.4 kJ mol^{-1}), and (Pd_wd)-ST (39.7 kJ mol^{-1}), reflecting that ST modification before Pd loading can effectively improve the catalytic performance. The E_a values of Pd_A, (Pd_A)-ST, and (Pd_wd)-ST were consistent with the reported E_a of Pd–CeO_2 catalysts in the literature[19,33] suggesting the same catalytic mechanism. Although the three catalysts exhibited similar catalytic performances at low temperatures (<40 °C), they performed differently at higher temperatures (Fig. S9†). The catalytic activities of (Pd_A)-ST and (Pd_wd)-ST were 1.5 times higher than that of Pd_A at 70 °C illustrating the performance enhancement by post-ST-modification on the composite catalyst, which was also similar to the phenomenon observed in the literature.[11,14] To further evaluate the performance of Pd_A-ST, we compared it with the reported Pd-/Pt-catalysts possessing low-temperature (<30 °C) catalytic activity in recent years (Fig. 1d and Table S1†) based on the mass specific activity at 27 °C.[11,15–20] Pd_A-ST exhibited a significantly higher mass specific activity of 9.72 $mol_{CO}\ h^{-1}\ g_{Pd}{}^{-1}$ at a high GHSV of 300 000 mL $h^{-1}\ g_{cat.}{}^{-1}$ than other Pd-/Pt-catalysts (<3 $mol_{CO}\ h^{-1}\ g_{metal}{}^{-1}$), highlighting the effectiveness and superiority of ST modification before loading of active metals.

2.2 Effects of steam treatment on the ceria structure

The structural properties of various ceria samples were investigated to elucidate the effects of ST on the structure and morphology of ceria supports. Steam-treated ceria (A-CeO_2-ST) maintained the original fluorite structure and rod-like morphology of as-synthesized ceria (A-CeO_2), as determined by powder X-ray diffraction (PXRD) and electron microscopy (Fig. 2 and S10†). The sharper diffraction peak of A-CeO_2-ST corresponded to a larger crystallite size (32 nm, Table 1) than that of A-CeO_2 (14.6 nm), indicating that ceria crystallinity was further enhanced under ST conditions. Additionally, the crystal constant of A-CeO_2-ST (0.5411 nm) was smaller than that of A-CeO_2 (0.5421 nm), which may be attributed to the reduced concentration of Ce^{3+} with a larger radius than Ce^{4+}. Since Ce^{3+} is always associated with oxygen defects,[34] Raman was used to verify the changes in defect concentration of ceria (Fig. S11†). As shown in Table 1, the defects in A-CeO_2-ST ($I_D/I_{F_{2g}} = 0.02$) were significantly lower than those of A-CeO_2 ($I_D/I_{F_{2g}} = 0.07$), possibly due to recrystallization or water occupation.

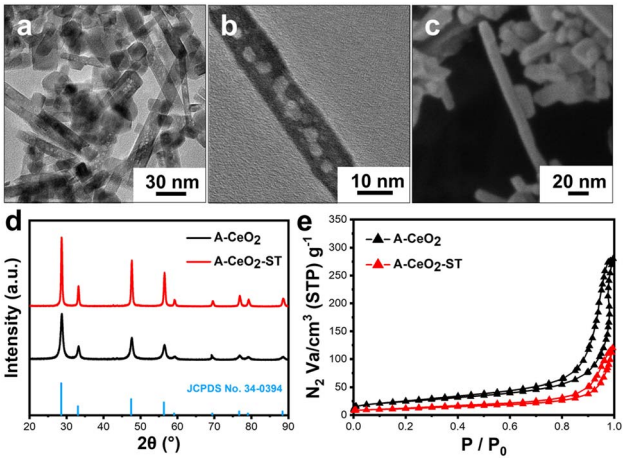

Fig. 2 (a and b) TEM and (c) SEM images of A-CeO_2-ST. (d) PXRD patterns of A-CeO_2 and A-CeO_2-ST. The bottom row is the standard diffraction patterns of the CeO_2 fluorite structure (JCPDS no. 34-0394). (e) Nitrogen adsorption–desorption curves of A-CeO_2 and A-CeO_2-ST.

In addition to the changes in crystallinity and defect concentration of A-CeO_2-ST, sintering phenomena were observed in transmission electron microscopy (TEM) when compared with A-CeO_2 (Fig. 2 and S10†). These sintering phenomena included rounded edges and particle agglomeration (Fig. 2a), resulting in a reduction of the specific surface area of A-CeO_2-ST (40.2 m^2 g^{-1}) by about half compared with that of A-CeO_2 (85.6 m^2 g^{-1}) (Fig. 2e and Table 1). It should be noted that there are a number of 2–4 nm pore structures on the A-CeO_2-ST (Fig. 2b), which were not found on A-CeO_2 (Fig. S10b†). However, no hole-like morphology was observed on the surface of A-CeO_2-ST using scanning electron microscopy (SEM) (Fig. 2c). Additionally, the pore volume of A-CeO_2-ST (0.19 mL g^{-1}) was significantly reduced compared to that of A-CeO_2 (0.44 mL g^{-1}). Thus, these pore structures inside A-CeO_2-ST were internal pores, ascribed to the defect movement and crystal rearrangement under high-temperature treatment conditions. A similar morphology of ceria was reported after calcination as well.[35] Since such internal pores did not contribute to the surface area or defect concentration of ceria samples, they shouldn't have any impact on the catalytic performance. To sum up, the ST process enhanced the crystallinity of ceria while reducing the specific surface area and defect concentration caused by sintering and recrystallization. These structural changes in the modified ceria, however, are usually considered to cause a decrease in the dispersity of precious metals and even

Table 1 Lattice constant, grain size, surface area, pore volume, and defects measurement of A-CeO_2 and A-CeO_2-ST

Sample	Lattice constant (nm)	Grain size (nm)	Surface area[c] (m^2 g^{-1})	Pore volume[c] (cm^3 g^{-1})	$I_D/I_{F_{2g}}$[d]
A-CeO_2	0.54211[a]	14.6[a]	85.6	0.44	0.07
A-CeO_2-ST	0.54117[b]	32.0[b]	40.2	0.19	0.02

[a] Data were obtained from PXRD Rietveld refinements analysis. Unweighted profile factor (R_p): 4.45%. Weighted profile factor (R_{wp}): 5.92%. [b] Data were obtained from PXRD Rietveld refinement analysis. R_p: 4.09%. R_{wp}: 5.76%. [c] From nitrogen adsorption–desorption analysis. [d] From Raman spectra analysis.

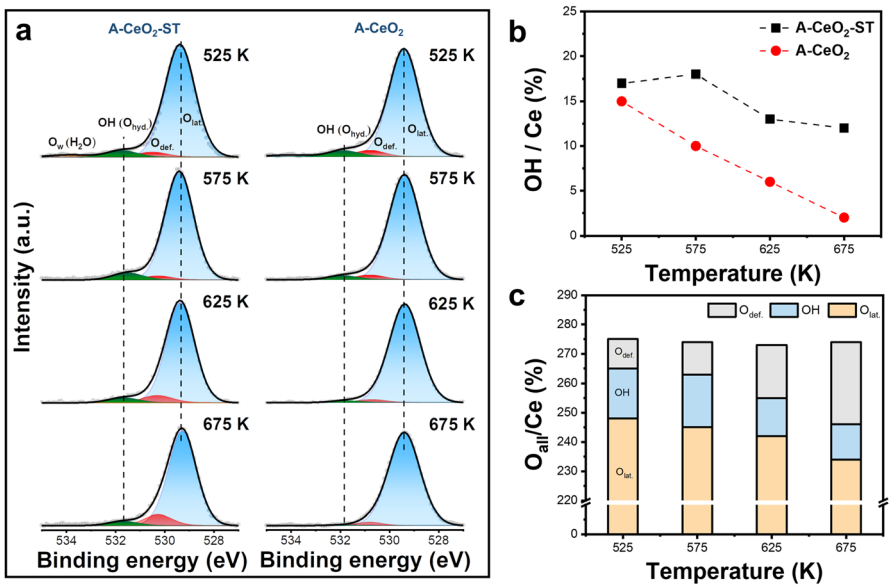

Fig. 3 (a) *In situ* XPS spectra of the O 1s core level of A-CeO_2-ST and A-CeO_2 at different temperatures under ultra-high vacuum. (b) The changing curves of the OH/Ce ratio of A-CeO_2 and A-CeO_2-ST, and (c) O_{all}/Ce ratio in the A-CeO_2-ST.

have adverse effects on catalytic oxidation reactions.[5,36,37] Therefore, the interaction between water and the ceria surface should be the key to regulating the properties of the ceria support.

Fourier transform infrared spectroscopy (FTIR) was conducted to detect changes of hydroxyl groups on the modified ceria (Fig. S12†). The vibration frequency of OH groups on the ceria is mainly distributed at 3500–3720 cm^{-1} in the FTIR spectrum.[38] Surprisingly, two obvious OH vibration peaks at 3612 cm^{-1} and 3648 cm^{-1} were observed in both A-CeO_2 and A-CeO_2-ST. The presence of OH groups in A-CeO_2 may be a residue of the hydrothermal synthesis process performed under high alkaline concentration conditions. To better compare the OH groups on the surface of the two samples, XPS was utilized for the semi-quantitative analysis of surface species (Fig. S13†). The O 1s peak can be deconvoluted into three peaks: lattice oxygen ($O_{lat.}$, 529.5 eV), defect-related oxygen ($O_{def.}$, 530.8 eV), and the OH group ($O_{hyd.}$, 531.6 eV).[39,40] The ratio of O_x/Ce (O_x: $O_{lat.}$, $O_{def.}$, $O_{hyd.}$) was used to evaluate the contents of each oxygen species in the ceria (Table S2†). The OH content in A-CeO_2 ($O_{hyd.}$/Ce: 0.22) was even higher than that in A-CeO_2-ST ($O_{hyd.}$/Ce: 0.15). Nevertheless, we believed that the OH groups on A-CeO_2 and A-CeO_2-ST were fundamentally different. Since A-CeO_2-ST was obtained through a high-temperature calcination, it is reasonable to speculate that the OH groups formed by ST have a certain degree of thermal stability. We used *in situ* XPS to investigate the change in surface oxygen species of ceria during the heating process and to confirm the stability of the OH groups. As the temperature increased from 525 to 675 K, residual OH groups on A-CeO_2 decreased rapidly ($O_{hyd.}$/Ce: 0.15 → 0.02) (Fig. 3a and b), whereas A-CeO_2-ST consistently maintained a relatively higher amount of OH groups ($O_{hyd.}$/Ce > 0.12). This phenomenon clearly proved that the OH groups formed on A-CeO_2-ST were more stable than the residual OH groups on A-CeO_2, possibly due to their different binding sites with the ceria. Further analysis of the oxygen species showed that the ratio of total oxygen to cerium (O_{all}/Ce) in A-CeO_2-ST consistently maintained a value about 2.74 during the heating process (Fig. 3c), while the ratio in A-CeO_2 greatly changed (Fig. S14†). The stable surface species ratio of A-CeO_2-ST was attributed to a more stable crystal structure after crystal recrystallization during the ST process, which agreed with the PXRD analysis. Moreover, the sum of the decrease of OH groups and $O_{lat.}$ was equal to the increase of $O_{def.}$ in A-CeO_2-ST (Fig. 3c), indicating that water was dissociated on the oxygen vacancies to form stable OH groups at high temperatures. However, both the OH groups and O_v in A-CeO_2 were significantly reduced during the heating process, and no direct correlation was observed.

In the ST process, high-temperature calcination could also affect the defect structure and stability of ceria.[41] To demonstrate that the presence of the OH groups is the major factor promoting catalytic performance, another control sample was prepared to calcine A-CeO_2 under the same ST conditions, but without steam, denoted as A-CeO_2-750, to investigate the calcination effects of A-CeO_2. The final obtained composite Pd catalyst was recorded as Pd_A-750. Structural characterization, including PXRD, Raman, and nitrogen adsorption–desorption, was conducted on A-CeO_2-750 as well (Fig. S15a–c†). The results showed that the lattice constant (0.54111 nm), grain size (31.1 nm), specific surface area (43.9 $m^2\ g^{-1}$), pore volume (0.26 mL g^{-1}), and defects ($I_D/I_{F_{2g}} = 0.02$) of A-CeO_2-750 were very similar to those of A-CeO_2-ST. However, the OH vibrational peak was obviously absent in the IR spectrum (Fig. S15d†). This indicated that the removal of OH groups was the main difference between A-CeO_2-750 and A-CeO_2-ST. We then tested the CO oxidation performance of Pd_A-ST and Pd_A-750. Pd_A-ST exhibited a significantly higher activity than Pd_A-750, with a reaction rate of 2.79 $mol_{CO}\ h^{-1}\ g_{Pd}{}^{-1}$ at 22 °C, which was 11 times more than that of Pd_A-750 (0.248 $mol_{CO}\ h^{-1}\ g_{Pd}{}^{-1}$ at 22 °C) (Fig. S16a†). However, we should consider that the factors influencing the performance of the composite catalyst are complex and multifaceted. For instance, changes in support properties can affect the MSI and metal dispersion,[6] leading to changes in activity, apart from the influence of OH groups on the reaction. To accurately evaluate the influence of OH groups without the interference of loaded metal, we carried out the performance tests on two pure supports, A-CeO_2-ST and A-CeO_2-750 (Fig. S16b†). The results were consistent with those of the composite catalysts; A-CeO_2-ST reached 98% conversion at 320 °C, while A-CeO_2-750 reached it at 370 °C. Obviously, OH groups had a more pronounced positive effect on promoting activity compared with the calcination effect. Overall, these results demonstrated that the ST process led to the formation of thermally stable OH groups on the surface oxygen defects of ceria, which is the key to enhancing the reactivity.

2.3 Effect of OH-modified ceria on Pd loading

In general, the properties of the support material can have a considerable impact on the MSI and are correlated with the stability, valence state, and interaction with reactants of metal active sites.[42–44] To gain a deeper understanding of the effect of A-CeO_2-ST on the loaded metals, we further explored the composite catalysts. All the composite catalysts (Pd_A-ST, Pd_A-750, and Pd_A) maintained a rod-like morphology with slight sintering (Fig. 4a, c and e). Neither Pd nor PdO was observed in PXRD patterns in all three samples (Fig. S17†), displaying high

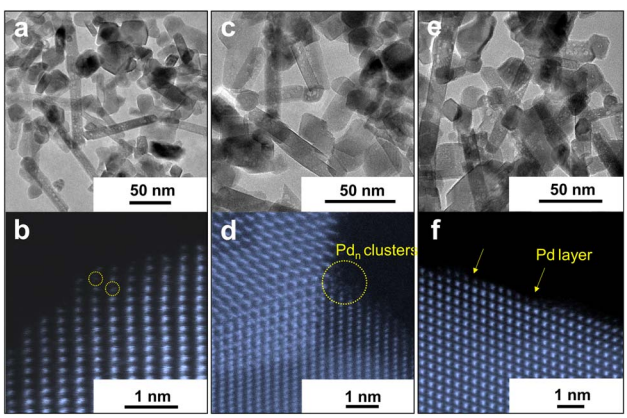

Fig. 4 TEM and spherical aberration-corrected HAADF-STEM images of (a and b) Pd_A-ST, (c and d) Pd_A-750, and (e and f) Pd_A.

dispersion or extremely small particle size of Pd species on the ceria supports.[45] Energy dispersive spectroscopy (EDS) analysis further confirmed that Pd species were highly dispersed in all samples (Fig. S18†). To investigate the state of small-sized metals on the surface, spherical aberration-corrected high-angle annular dark-field scanning transmission electron microscopy (HAADF-STEM) was performed to observe the differences in the three samples at an atomic level. Pd clusters were observed on both Pd_A and Pd_A-750 (Fig. 4d, f and S19d–i†), while no clusters were found on Pd_A-ST (Fig. 4b and S19a–c†), implying atomic dispersity of Pd on A-CeO_2-ST. Atomic intensity change analysis was performed to infer the most likely positions of Pd single atoms on the A-CeO_2-ST surface, which were highlighted with yellow circles. In addition to Pd clusters, a thin layer of Pd was also found on the surface of Pd_A (Fig. 4f and S19i†). A similar metal layer has been reported on the Cu–CeO_2 catalyst,[46] which was mainly caused by the MSI during the heat treatment process. The driving force for this phenomenon was the reduction of surface energy.[6] The varying Pd loading states, including Pd_1 on A-CeO_2-ST, Pd_n (~10 atoms) on A-CeO_2-750, Pd_n (~3 atoms) and the Pd layer on A-CeO_2, reflected the distinct differences in MSI between Pd and different ceria supports.

In addition to metal dispersion, MSI can also affect the degree of charge transfer between metals and supports, leading to changes in the valence states.[44] To probe this, we performed XPS of the Pd 3d core line (Fig. S20†). The decreasing order of Pd^{2+} BE in the three samples is Pd_A-ST (338.2 eV) > Pd_A (337.8 eV) > Pd_A-750 (337.3 eV), indicating that the corresponding MSI follows a trend of Pd_A-ST > Pd_A > Pd_A-750. The stronger MSI of Pd_A-ST than the other two samples ensured the stability of highly dispersed metal atoms. The result demonstrated the additional advantages of utilizing OH-modified ceria to achieve a high dispersion state. Furthermore, Pd_A-ST only possessed one Pd^{2+} species (Fig. S20†), while both Pd_A-750 and Pd_A had three types of Pd species (Pd^{2+}, $Pd^{\delta+}$, and Pd^0), reflecting a more complex loading scenario ascribed to the weaker MSI. In addition to Pd^{2+}, the $Pd^{\delta+}$ (336.1 eV) of Pd_A was also shifted to a higher BE than that of Pd_A-750 ($Pd^{\delta+}$: 335.5 eV). The enhanced MSI of Pd_A may be a result of the formation of the Pd layer structure. In a word, changes in support properties can disturb the loading state of metals through MSI, exhibiting different metal dispersion and valence states.

The catalyst with strong MSI typically tends to have strong binding affinity with the reactants, but it is also accompanied by surface poisoning for certain reactants, such as CO, which limits the low-temperature reactivity.[14,47] However, the strong MSI and high CO oxidation activity can be both observed in Pd_A-ST. To figure out the reason, a careful CO adsorption experiment was performed to explore the influence of the steam-modified ceria on Pd–CO adsorption strength. We combined chemical adsorption, chemical calorimetry, and mass spectrometer devices (Fig. 5a). This combination study could accurately measure the amount of CO adsorbed and the heat released when CO passes through the sample. A mass spectrometer was used to monitor the testing process which did not involve any chemical reactions. Our results showed that no CO_2 signal was generated during the test for any of the samples (Fig. 5b, S21a and b†), indicating that the process of CO molecules passing through the catalyst without oxygen was purely an adsorption process on the composite catalyst at 25 °C. Besides the Pd–CeO_2 composite samples, pure ceria supports were also tested in the CO adsorption experiment (Fig. S21c†). We found that the CO adsorption on all ceria supports at 25 °C was

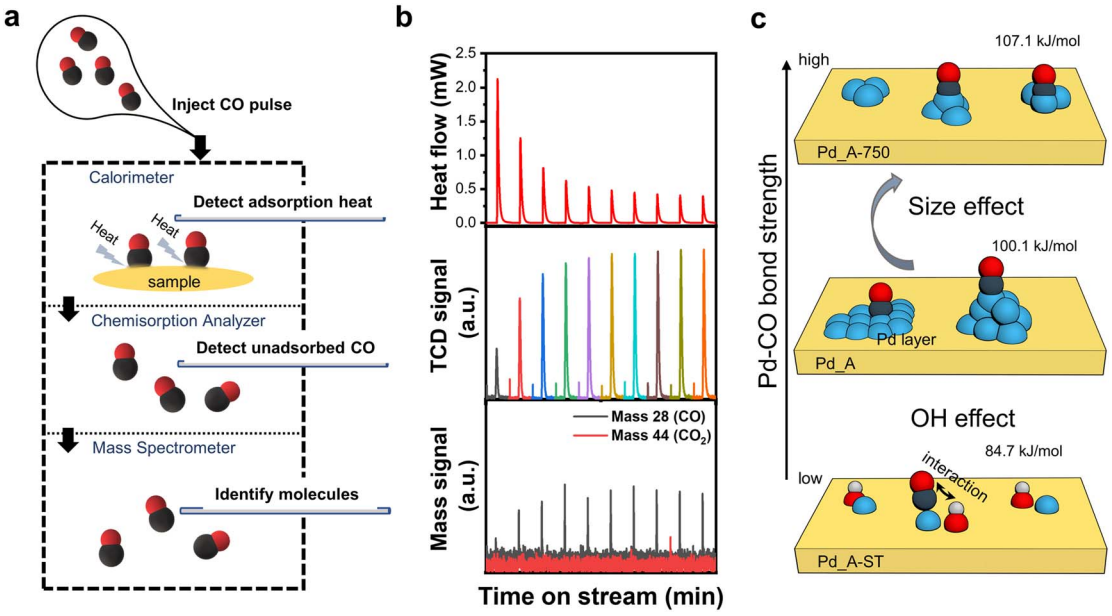

Fig. 5 (a) Schematic diagram of the combination of calorimeter–chemisorption analyzer–mass spectrometer devices. (b) Detection of the CO adsorption heat, unadsorbed amount of CO, and molecular mass. (c) Schematic diagram of structure and CO adsorption strength of Pd_A-ST, Pd_A-750, and Pd_A.

extremely weak, about one-thousandth of that on Pd-loaded catalysts. After subtracting the effect of the ceria support and calculating the adsorption energy required to form Pd–CO, the adsorption amount and normalized adsorption heat are shown in Table S3.† The energy emitted during the formation of Pd–CO on Pd_A-ST was 84.7 kJ mol^{-1}, which was lower than that of Pd_A (100.1 kJ mol^{-1}) and Pd_A-750 (107.1 kJ mol^{-1}). This result suggested that the high CO oxidation activity of Pd_A-ST may come from low CO affinity, and the A-CeO_2-ST support weakened the binding strength between the loaded Pd and CO molecules, although A-CeO_2-ST can strongly interact with Pd. According to the reported relationship between the adsorption energy and Pd size,[48] the adsorption energy increases as the metal size decreases when the effective diameter of Pd is less than 2 nm, which explains the stronger adsorption energy of Pd_A-750 (~3 atoms Pd) compared to Pd_A (~10 atoms) (Fig. 5c). However, atomically dispersed Pd_A-ST did not exhibit stronger adsorption, which could be attributed to the influence of OH groups.[49,50] In brief, OH not only regulated the surface properties of the ceria support, which improved the dispersion of metals, but also weakened the adsorption strength of CO on Pd_A-ST, thereby lowering the activation energy and ultimately achieving high reactivity.

3. Conclusions

In summary, we proposed a strategy to regulate the MSI of the Pd–CeO_2 composite catalyst by modifying the ceria support with steam treatment before loading metals. This strategy effectively reduced the activation energy of CO oxidation (11.6 kJ mol^{-1}) and achieved high reactivity (9.72 mol_{CO} h^{-1} $g_{Pd}{}^{-1}$) at room temperature (27 °C). High ST temperature and a certain defect concentration of CeO_2 were the key factors in improving catalytic activity. Crystallographic characterization and *in situ* XPS analysis revealed that thermally stable OH groups were formed on the oxygen defects of ceria during the ST process. The cross control experiments confirmed that the OH groups were the dominant factor for improving catalyst activity. HADDF-STEM and XPS analysis demonstrated that OH-modified ceria influenced the Pd dispersion and valence state, reflecting the regulation of MSI. Binding strength testing revealed that the adsorption energy of Pd–CO (84.7 kJ mol^{-1}) was weakened on the Pd catalyst with OH-modified ceria, supporting the low activation energy of CO oxidation at low temperatures. This study demonstrates the significant impact of support modification on the MSI and catalytic performance of composite catalysts and provides a foundation for developing more efficient metal catalysts.

Author contributions

Y. A. performed most sample synthesis, catalytic tests, material characterization (TEM, XPS, adsorption heat, and other characterization tests), data analysis, and article writing. S.-Y. C. participated in the construction of the catalytic system, data analysis, and article revision. B. W. performed *in situ* XPS experiments and XPS analysis guidance. L. Z., Y. W. and G. H. performed supplementation data. J. C. participated in the discussion and revision of the article. Z. L. and L.-Y. C. provided major guidance, construction of the research idea, and article revision. C.-K. T. initiated and led this project. The manuscript was written through contributions of all authors. All authors have given approval to the final version of the manuscript.

Conflicts of interest

There are no conflicts to declare.

Acknowledgements

This work was supported by the start-up funding from ShanghaiTech University. This work was partially supported by the Center of high-resolution Electron Microscopy (CℏEM) of the SPST at ShanghaiTech under grant EM02161943. Z. L. is partially supported by Shanghai high repetition rate XFEL and extreme light facility (SHINE). The authors thank BLO2B01 of the Shanghai Synchrotron Radiation Facility and lab-based SPECS AP-XPS instrument supported by the National Natural Science Foundation of China, No. 11227902. The authors thank Dr Zheng Peng, Peihong Cheng, Haiyin Zhu, Qing Zhang, Lili Du, and Na Yu for their assistance in characterization. The authors thank Dr Xiangwen Liu for assistance with sample synthesis.

Notes and references

1 A. Trovarelli, *Catalysis by Ceria and Related Materials*, World Scientific, Singapore, 2002.
2 Q. Wang, K. L. Yeung and M. A. Bañares, *Catal. Today*, 2020, **356**, 141–154.
3 X. Huang, K. Zhang, B. Peng, G. Wang, M. Muhler and F. Wang, *ACS Catal.*, 2021, **11**, 9618–9678.
4 T. Montini, M. Melchionna, M. Monai and P. Fornasiero, *Chem. Rev.*, 2016, **116**, 5987–6041.
5 J. A. Farmer and C. T. Campbell, *Science*, 2010, **329**, 933–936.
6 T. W. van Deelen, C. H. Mejía and K. P. de Jong, *Nat. Catal.*, 2019, **2**, 955–970.
7 X. Liu, K. Zhou, L. Wang, B. Wang and Y. Li, *J. Am. Chem. Soc.*, 2009, **131**, 3140–3141.
8 R. Si and M. Flytzani-Stephanopoulos, *Angew. Chem., Int. Ed.*, 2008, **120**, 2926–2929.
9 F. Jiang, S. Wang, B. Liu, J. Liu, L. Wang, Y. Xiao, Y. Xu and X. Liu, *ACS Catal.*, 2020, **10**, 11493–11509.
10 M. G. Jang, S. Yoon, D. Shin, H. J. Kim, R. Huang, E. Yang, J. Kim, K.-S. Lee, K. An and J. W. Han, *ACS Catal.*, 2022, **12**, 4402–4414.
11 H. Jeong, J. Bae, J. W. Han and H. Lee, *ACS Catal.*, 2017, **7**, 7097–7105.
12 L. Ma, C. Ding, Z. Ma, J. Wang, H. Xu, K. Zhang and G. Li, *Int. J. Hydrogen Energy*, 2023, **48**, 17055–17064.
13 B.-J. Wang, J.-P. Zhang, Y. Han, Y.-K. Gao, G.-L. Xiang, G.-W. Chu and Y. Luo, *ACS Eng. Au*, 2022, **2**, 486–495.

14 L. Nie, D. Mei, H. Xiong, B. Peng, Z. Ren, X. I. P. Hernandez, A. Delariva, M. Wang, M. H. Engelhard, L. Kovarik, A. K. Datye and Y. Wang, *Science*, 2017, **358**, 1419–1423.
15 H. Jeong, D. Shin, B. S. Kim, J. Bae, S. Shin, C. Choe, J. W. Han and H. Lee, *Angew. Chem., Int. Ed.*, 2020, **132**, 20872–20877.
16 B. Qiao, A. Wang, X. Yang, L. F. Allard, Z. Jiang, Y. Cui, J. Liu, J. Li and T. Zhang, *Nat. Chem.*, 2011, **3**, 634–641.
17 S. Gatla, D. Aubert, G. Agostini, O. Mathon, S. Pascarelli, T. Lunkenbein, M. G. Willinger and H. Kaper, *ACS Catal.*, 2016, **6**, 6151–6155.
18 Y. Xia, J. Ye, D.-g. Cheng, F. Chen and X. Zhan, *Catal. Sci. Technol.*, 2018, **8**, 5137–5147.
19 Z. Hu, X. Liu, D. Meng, Y. Guo, Y. Guo and G. Lu, *ACS Catal.*, 2016, **6**, 2265–2279.
20 H. Jeong, O. Kwon, B.-S. Kim, J. Bae, S. Shin, H.-E. Kim, J. Kim and H. Lee, *Nat. Catal.*, 2020, **3**, 368–375.
21 M. Fronzi, S. Piccinin, B. Delley, E. Traversa and C. Stampfl, *Phys. Chem. Chem. Phys.*, 2009, **11**, 9188–9199.
22 M. Molinari, S. C. Parker, D. C. Sayle and M. S. Islam, *J. Phys. Chem. C*, 2012, **116**, 7073–7082.
23 F. Esch, S. Fabris, L. Zhou, T. Montini, C. Africh, P. Fornasiero, G. Comelli and R. Rosei, *Science*, 2005, **309**, 752–755.
24 X. I. Pereira-Hernández, A. DeLaRiva, V. Muravev, D. Kunwar, H. Xiong, B. Sudduth, M. Engelhard, L. Kovarik, E. J. Hensen and Y. Wang, *Nat. Commun.*, 2019, **10**, 1–10.
25 J. Jones, H. Xiong, A. T. DeLaRiva, E. J. Peterson, H. Pham, S. R. Challa, G. Qi, S. Oh, M. H. Wiebenga, X. I. Pereira Hernández, Y. Wang and A. K. Datye, *Science*, 2016, **353**, 150–154.
26 D. Jiang, G. Wan, C. E. Garcia-Vargas, L. Li, X. I. Pereira-Hernandez, C. Wang and Y. Wang, *ACS Catal.*, 2020, **10**, 11356–11364.
27 C. Schilling, A. Hofmann, C. Hess and M. V. Ganduglia-Pirovano, *J. Phys. Chem. C*, 2017, **121**, 20834–20849.
28 A. Filtschew, K. Hofmann and C. Hess, *J. Phys. Chem. C*, 2016, **120**, 6694–6703.
29 V. Muravev, G. Spezzati, Y.-Q. Su, A. Parastaev, F.-K. Chiang, A. Longo, C. Escudero, N. Kosinov and E. J. Hensen, *Nat. Catal.*, 2021, **4**, 469–478.
30 P. G. Lustemberg, P. J. Ramírez, Z. Liu, R. A. Gutierrez, D. G. Grinter, J. Carrasco, S. D. Senanayake, J. A. Rodriguez and M. V. Ganduglia-Pirovano, *ACS Catal.*, 2016, **6**, 8184–8191.
31 Y. Chen, J. Chen, W. Qu, C. George, M. Aouine, P. Vernoux and X. Tang, *Chem. Commun.*, 2018, **54**, 10140–10143.
32 A. I. Boronin, E. M. Slavinskaya, I. G. Danilova, R. V. Gulyaev, Y. I. Amosov, P. A. Kuznetsov, I. A. Polukhina, S. V. Koscheev, V. I. Zaikovskii and A. S. Noskov, *Catal. Today*, 2009, **144**, 201–211.
33 M. Cargnello, V. V. Doan-Nguyen, T. R. Gordon, R. E. Diaz, E. A. Stach, R. J. Gorte, P. Fornasiero and C. B. Murray, *Science*, 2013, **341**, 771–773.
34 C. Yang, Y. Lu, L. Zhang, Z. Kong, T. Yang, L. Tao, Y. Zou and S. Wang, *Small Struct.*, 2021, **2**, 2100058.
35 T. S. Sakthivel, D. L. Reid, U. M. Bhatta, G. Möbus, D. C. Sayle and S. Seal, *Nanoscale*, 2015, **7**, 5169–5177.
36 S. Chang, M. Li, Q. Hua, L. Zhang, Y. Ma, B. Ye and W. Huang, *J. Catal.*, 2012, **293**, 195–204.
37 Q.-L. Zhu and Q. Xu, *Chem*, 2016, **1**, 220–245.
38 K. Hadjiivanov, *Adv. Catal.*, 2014, **57**, 99–318.
39 F. Liang, Y. Yu, W. Zhou, X. Xu and Z. Zhu, *J. Mater. Chem. A*, 2015, **3**, 634–640.
40 C. Yang, X. Yu, S. Heißler, A. Nefedov, S. Colussi, J. Llorca, A. Trovarelli, Y. Wang and C. Wöll, *Angew. Chem., Int. Ed.*, 2017, **56**, 375–379.
41 F. Lin, K. Rappé, L. Kovarik, M. Song, X. S. Li, M. Engelhard and Y. Wang, *Catal. Sci. Technol.*, 2022, **12**, 2462–2470.
42 W.-W. Wang, W.-Z. Yu, P.-P. Du, H. Xu, Z. Jin, R. Si, C. Ma, S. Shi, C.-J. Jia and C.-H. Yan, *ACS Catal.*, 2017, **7**, 1313–1329.
43 A. Parastaev, V. Muravev, E. H. Osta, A. J. van Hoof, T. F. Kimpel, N. Kosinov and E. J. Hensen, *Nat. Catal.*, 2020, **3**, 526–533.
44 O. Bezkrovnyi, A. Bruix, D. Blaumeiser, L. Piliai, S. Schötz, T. Bauer, I. Khalakhan, T. Skala, P. Matvija, P. Kraszkiewicz, M. Pawlyta, M. Vorokhta, I. Matolínová, J. Libuda, K. M. Neyman and L. Kępiński, *Chem. Mater.*, 2022, **34**, 7916–7936.
45 L. Zhang, R. Chen, Y. Tu, X. Gong, X. Cao, Q. Xu, Y. Li, B. Ye, Y. Ye and J. Zhu, *ACS Catal.*, 2023, **13**, 2202–2213.
46 B. Wang, H. Zhang, W. Xu, X. Li, W. Wang, L. Zhang, Y. Li, Z. Peng, F. Yang and Z. Liu, *ACS Catal.*, 2020, **10**, 12385–12392.
47 K. Ding, A. Gulec, A. M. Johnson, N. M. Schweitzer, G. D. Stucky, L. D. Marks and P. C. Stair, *Science*, 2015, **350**, 189–192.
48 I. V. Yudanov, A. Genest, S. Schauermann, H.-J. Freund and N. Rösch, *Nano Lett.*, 2012, **12**, 2134–2139.
49 J. Saavedra, H. A. Doan, C. J. Pursell, L. C. Grabow and B. D. Chandler, *Science*, 2014, **345**, 1599–1602.
50 C. Wang, X.-K. Gu, H. Yan, Y. Lin, J. Li, D. Liu, W.-X. Li and J. Lu, *ACS Catal.*, 2017, **7**, 887–891.